β-globin plasmid; S. Shenoy (Albert Einstein College of Medicine), L. Gelman and S. Bourke (Friedrich Miescher Institute), and EMBL Advanced Light Microscopy Facility for microscopy support; D. Ciepielewski (Nikon) for providing access to NIS tracking software; C. Eliscovich (Albert Einstein College of Medicine) for advice on IF-FISH; L. Lavis (Janelia Farm) for providing JF_{549} dye; M. Beal (Biosearch Technologies) for Stellaris FISH probes; A. Arnold (FMI) for assistance with polysome analysis; I. Gáspár (EMBL) for pHsp83 vector; and S. Chao, U. Meier, and J. Warner for helpful discussions.

SUPPLEMENTARY MATERIALS

www.sciencemag.org/content/347/6228/1367/suppl/DC1
Materials and Methods
Figs. S1 to S12
Movies S1 to S7
References (*28*–*37*)

20 November 2014; accepted 6 February 2015
10.1126/science.aaa3380

RNA BIOCHEMISTRY

Determination of in vivo target search kinetics of regulatory noncoding RNA

Jingyi Fei,[1] Digvijay Singh,[2] Qiucen Zhang,[1] Seongjin Park,[1] Divya Balasubramanian,[3] Ido Golding,[1,4] Carin K. Vanderpool,[3*] Taekjip Ha[1,2,5,6*]

Base-pairing interactions between nucleic acids mediate target recognition in many biological processes. We developed a super-resolution imaging and modeling platform that enabled the in vivo determination of base pairing–mediated target recognition kinetics. We examined a stress-induced bacterial small RNA, SgrS, which induces the degradation of target messenger RNAs (mRNAs). SgrS binds to a primary target mRNA in a reversible and dynamic fashion, and formation of SgrS-mRNA complexes is rate-limiting, dictating the overall regulation efficiency in vivo. Examination of a secondary target indicated that differences in the target search kinetics contribute to setting the regulation priority among different target mRNAs. This super-resolution imaging and analysis approach provides a conceptual framework that can be generalized to other small RNA systems and other target search processes.

Base-pairing interactions between nucleic acids constitute a large category of target recognition processes such as noncoding RNA-based gene regulation [e.g., microRNAs (*1*) and long noncoding RNAs (*2*) in eukaryotes and small RNAs (sRNAs) in bacteria (*3*)], bacterial adaptive immunity [e.g., the clustered regularly interspaced short palindromic repeat (CRISPR) system (*4*)], and homologous recombination (*5*). Although target search kinetics by transcription factors has been studied in vivo (*6*), the rate constants for target identification via base-pairing interactions in vivo are not known for any system. Here, we developed a super-resolution imaging and analysis platform to assess the kinetics of base-pairing interaction-mediated target recognition for a bacterial sRNA, SgrS. SgrS is produced upon sugar-phosphate stress, and its function is dependent on an RNA chaperone protein Hfq. SgrS regulates several target mRNAs posttranscriptionally through base-pairing interactions that affect mRNA translation and stability (*7*). We combined single-molecule fluorescence in situ hybridization (smFISH) (*8*) with single-molecule localization-based super-resolution microscopy (*9*) to count RNAs and obtain information on subcellular localization. High spatial resolution is required for accurate quantification of the high-copy-number RNAs and sRNA-mRNA complexes. Here, simultaneous measurements of sRNA, mRNA, and sRNA-mRNA complexes together with mathematical modeling allow determination of key parameters describing sRNA target search and downstream codegradation of sRNA-mRNA complexes.

We first studied the kinetic properties of SgrS regulation of *ptsG* mRNA, encoding a primary glucose transporter. SgrS binds within the 5′ untranslated region (UTR) of *ptsG* mRNA, blocks its translation, and induces its degradation (*10*). We induced stress and SgrS production in *Escherichia coli* strains derived from wild-type MG1655 (table S1) using a nonmetabolizable sugar analog, α-methyl glucoside (αMG) (*10*, *11*). Fractions of cell culture were taken at different time points after induction and fixed (*12*). Oligonucleotide probes (table S2) labeled with photoswitchable dyes, Alexa 647 and Alexa 568, were used to detect SgrS (9 probes) and *ptsG* mRNA (28 probes), respectively, using smFISH (*8*). We then imaged the cells using two-color three-dimensional (3D) super-resolution microscopy (*9*, *12*) (Fig. 1A; compare to diffraction limited images in Fig. 1B).

In the wild-type strain (table S1), we observed production of SgrS and corresponding reduction of *ptsG* mRNA over a few minutes (Fig. 1A), consistent with SgrS-mediated degradation of *ptsG* mRNA (*10*). In a strain producing an SgrS that does not base pair with *ptsG* mRNA due to mutations in the seed region (*13*, *14*) and in an Hfq deletion (Δ*hfq*) strain (table S1), *ptsG* mRNA reduction was not observed (figs. S1 and S2). To quantify the copy number of RNAs in each cell, we employed a density-based clustering algorithm to map single-molecule localization signal to individual clusters corresponding to individual RNAs (*12*, *15*, *16*) (Fig. 1C and movies S1 and S2). The absolute copy number quantification was validated by quantitative polymerase chain reaction (qPCR) (*12*) (Fig. 1D).

We next built a kinetic model containing the following kinetic steps: transcription of SgrS (with rate constant α_S) and *ptsG* (α_p), endogenous degradation of *ptsG* mRNA (with rate constant β_p), degradation of SgrS in the absence of codegradation with *ptsG* mRNA ($\beta_{S,p}$), binding of SgrS to *ptsG* mRNA (with rate constant k_{on}), dissociation of SgrS from *ptsG* mRNA (k_{off}), and ribonuclease E (RNase E)–mediated codegradation of SgrS-*ptsG* mRNA complex (k_{cat}) (Fig. 1E). We independently measured β_p and the total SgrS degradation rate, including endogenous and mRNA-coupled degradation [table S4, fig. S3, and supplementary materials section 1.9 (SM 1.9)]. Because *ptsG* mRNA levels remained constant in the absence of SgrS-mediated degradation, as observed in the base-pairing mutant strain (fig. S1), we determined α_p as the product of β_p and *ptsG* mRNA concentration before SgrS induction (table S4 and SM 1.10)

To determine k_{on} and k_{off}, it is necessary to count the SgrS-*ptsG* mRNA complexes. Colocalization of *ptsG* mRNA and SgrS at the 40-nm resolution was rarely observed in the wild-type strain (up to ~5%, similar to ~3% colocalization by chance, estimated using the base-pairing mutant as a negative control) (Fig. 2). This is possibly because SgrS regulates several other target mRNAs (*7*) and/or the SgrS-*ptsG* mRNA complex may be unstable due to rapid codegradation or disassembly. In an RNase E mutant strain, in which codegradation is blocked (*17*, *18*) (table S1), *ptsG* mRNA levels stayed the same as SgrS levels increased (fig. S4) (*17*, *18*), and a fraction of *ptsG* mRNA colocalized with SgrS, increasing over time to reach ~15% (Fig. 2 and fig. S5). A positive control using *ptsG* mRNA simultaneously labeled with two colors (Fig. 2 and SM 1.8) showed a high degree of colocalization (~70%), similar to the reported detection efficiency of colocalization by super-resolution imaging (*19*).

We then applied these measured parameters (α_p and β_p), used total SgrS degradation rate as a constraint for $\beta_{S,p}$, and determined the remaining parameters (α_S, $\beta_{S,p}$ k_{on}, k_{off}, and k_{cat}) by fitting equations (Fig. 1E) to the six time-course changes of SgrS, *ptsG* mRNA, and SgrS-*ptsG* mRNA complex in both the wild-type and the RNase E mutant strains (Fig. 3A, table S4, and SM 1.10). We further validated the model by changing

---

[1]Center for the Physics of Living Cells, Department of Physics, University of Illinois, Urbana, IL, USA. [2]Center for Biophysics and Computational Biology, University of Illinois, Urbana, IL, USA. [3]Department of Microbiology, University of Illinois, Urbana, IL, USA. [4]Verna and Marrs McLean Department of Biochemistry and Molecular Biology, Baylor College of Medicine, Houston, TX, USA. [5]Carl R. Woese Institute for Genomic Biology, Howard Hughes Medical Institute, Urbana, IL, USA. [6]Howard Hughes Medical Institute, Urbana, IL, USA.
***Corresponding author. E-mail: tjha@illinois.edu (T.H.); cvanderp@life.uiuc.edu (C.K.V.)**

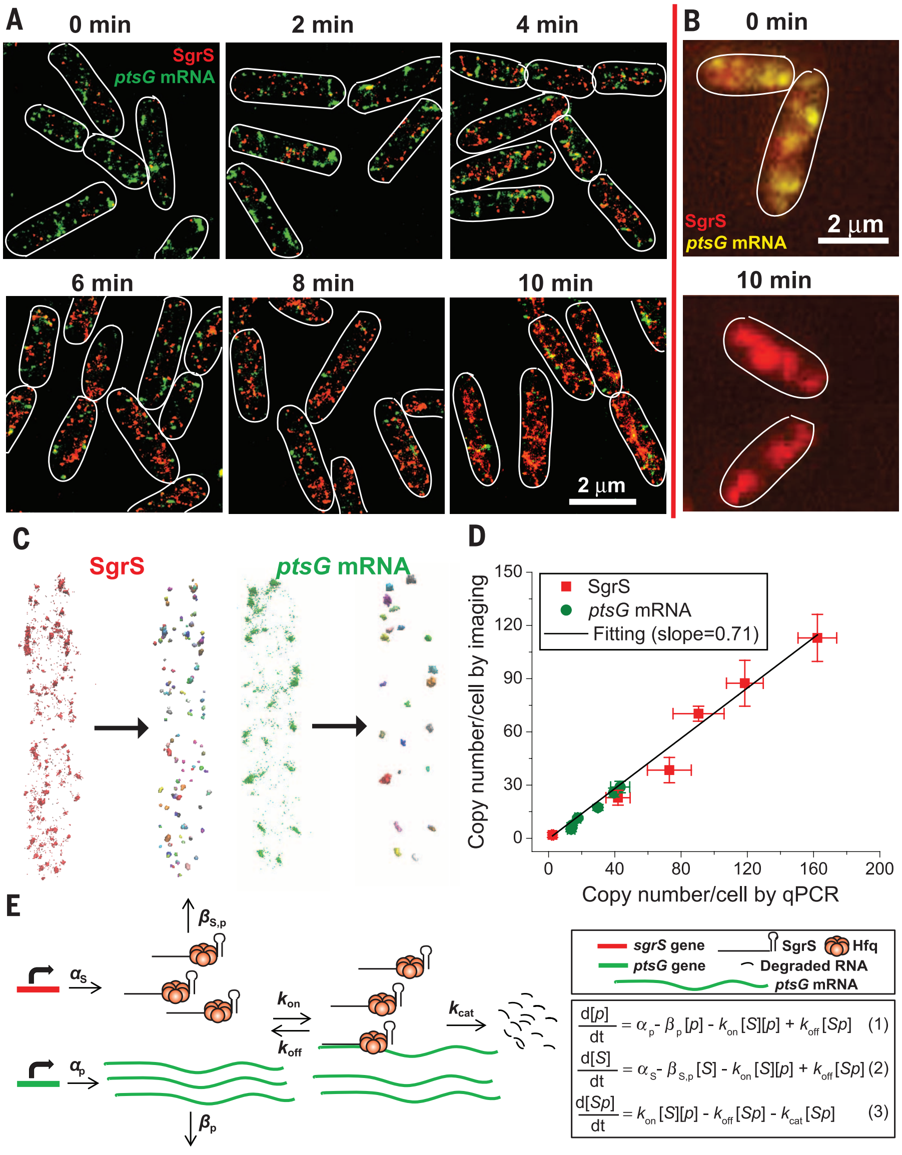

Fig. 1. Super-resolution imaging and analysis. (**A**) 3D Super-resolution images of SgrS and *ptsG* mRNA labeled by smFISH projected in 2D planes. (**B**) Diffraction-limited fluorescent images of SgrS and *ptsG* mRNA. Cell boundaries imaged by differential interference contrast in (A) and (B) are depicted by white solid lines. (**C**) Examples of clustering analysis with comparison of raw data (left) and clustered data (right). (**D**) Comparison of average RNA copy number per cell measured by super-resolution imaging and qPCR. (**E**) Kinetic scheme of SgrS-induced *ptsG* mRNA degradation. Kinetic steps are described in the main text. [*p*], [*S*], and [*Sp*] are the concentrations of *ptsG* mRNA, SgrS, and their complex, respectively, in the mass-action equations.

experimental conditions to vary only the transcription rates of SgrS (with lower αMG concentration) and/or *ptsG* mRNA (in the absence of glucose in the growth media), and the model could account for the data with the same set of k_{on}, k_{off}, and k_{cat} values (table S4, figs. S6 to S8, and SM 2.2).

We can now quantitatively examine the effect of Hfq, which functions by stabilizing the sRNA or promoting its annealing with the target mRNA (*20*). In the Δ*hfq* strain, the degradation rate of SgrS increased by a factor of 20, whereas the SgrS-*ptsG* mRNA association rate decreased slightly (table S4, figs. S1 and S8, and SM 2.2). Therefore, for the SgrS-ptsG mRNA pair, the primary effect of Hfq in regulation kinetics is in SgrS stabilization.

This in vivo determination of base pairing–mediated target search kinetics revealed two important characteristics of SgrS-mediated *ptsG* mRNA degradation. First, the target search process is characterized by slow association [k_{on} = (2.0 ± 0.2) × 10^5 M^{-1} s^{-1}] and fast dissociation (k_{off} = 0.20 ± 0.04 s^{-1}), resulting in a dissociation constant (K_D = k_{off}/k_{on}) of 1.0 ± 0.2 μM (Fig. 3B and SM 1.11). To get a comparable apparent association rate, $k_{a,app}$ (k_{on}×[S]), and k_{off}, about one thousand SgrS molecules per cell need to be produced. The large K_D explains the need for excessive production of sRNA molecules to enable rapid regulation when cells experience high levels of stress. Despite the crowded cellular environment and large excess of non–target RNA molecules, the k_{on} is within the wide range of Hfq-mediated sRNA and target mRNA association rates reported by in vitro measurements. In contrast, k_{off} is 1 to 2 orders of magnitude larger than in vitro estimates (*21*–*23*). The large K_D for target search in vivo is likely due to the limited availability of key players in the cell. For example, Hfq was suggested to be limited in the cell due to the dynamic competition for Hfq among different sRNAs (*24*, *25*). Second, k_{cat} and k_{off} are comparable such that both codegradation and dissociation can occur with similar probabilities upon target binding. Disallowing dissociation by setting k_{off} to zero cannot explain our experimental data (fig. S9 and SM 2.1). The observed fast k_{cat} (0.4 ± 0.1 s^{-1}) may be due to the formation of a ribonucleoprotein complex comprised of SgrS, Hfq, and RNase E, as suggested by biochemical studies (*18*); if so, once SgrS-Hfq-RNase E binds the *ptsG* mRNA, RNase E would be readily available for codegradation.

The kinetic model suggests that the overall rate of *ptsG* mRNA degradation is limited by its association with SgrS: At early time points after SgrS induction, when the copy number of SgrS is on the order of tens per cell, $k_{a,app}$ is about two orders of magnitude smaller than the codegradation rate k_{cat}. The nonhomogenous spatial distribution of the sRNA and its target mRNA may also contribute to the slow target search. We observed membrane localization of *ptsG* mRNA, whereas SgrS is primarily localized in the cytoplasm (fig. S10). Further modeling incorporating the spatial information and stochastic gene expression may improve the kinetic analysis.

Regulation prioritization among multiple targets by one sRNA was suggested by computational modeling (*26*, *27*) and experimental observation (*28*). However, how the kinetic prioritization is achieved remains to be elucidated. We propose that the combination of k_{on}, k_{off}, and k_{cat} is characteristic of a specific sRNA-mRNA pair and determines the regulatory outcome. k_{cat} may reflect the regulatory mode (codegradation versus translation repression) and target search kinetics (k_{on} and k_{off}) could contribute to the regulatory specificity and priority among many targets. To investigate this possibility, we examined *manXYZ* mRNA, which encodes a general sugar transporter for mannose and glucose and is also negatively regulated by SgrS. Compared with *ptsG*, *manXYZ* mRNA showed slower degradation kinetics (*28*) (figs. S11 to S13). The prioritization of *ptsG* over *manXYZ* by SgrS is consistent with the observation that SgrS regulation of *ptsG* (but not *manXYZ*) is absolutely essential for continued cell growth under most stress conditions (*29*). Using the RNase E mutant strain, we found that formation of SgrS-*manXYZ* mRNA complexes is slower than SgrS-*ptsG* mRNA complex formation (fig. S13C). The K_D for SgrS binding to *manXYZ* mRNA, 2.3 ± 0.2 μM, was also higher than 1.0 ± 0.2 μM for SgrS binding to *ptsG* mRNA (Fig. 3B and SM 1.11). This result indicates that the slower regulation kinetics observed for *manXYZ* may, at least partially, originate from the differences in target search kinetics.

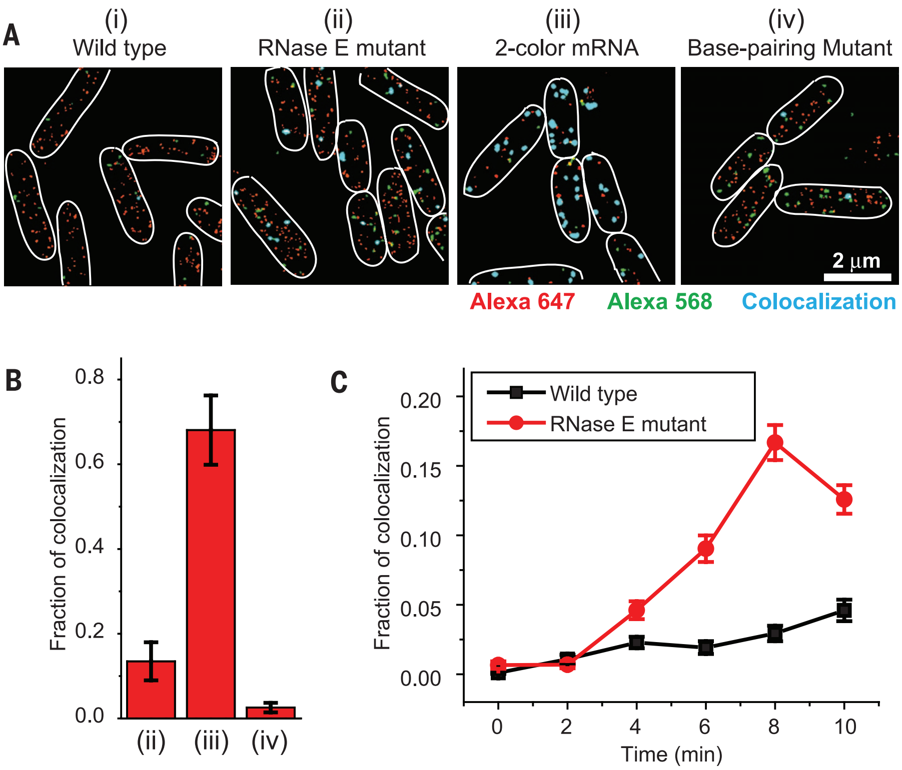

Fig. 2. Colocalization analysis of SgrS-*ptsG* complex. (**A**) Example of colocalization under various conditions. (**B**) Quantification of colocalized fraction of *ptsG* mRNA in cases (ii), (iii) (at 10 min after SgrS induction), and (iv) (at 10 min after SgrS induction). Error bars are standard deviations from three to eight images. (**C**) Time-course changes in the fraction of colocalized *ptsG* mRNA with SgrS. Error bars are standard errors from 200 to 600 cells from two independent measurements.

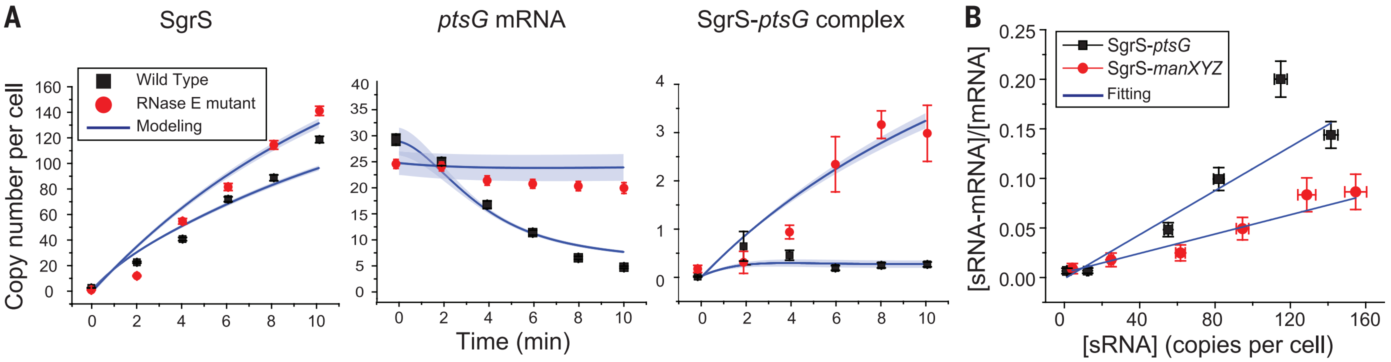

Fig. 3. Estimation of kinetic parameters. (**A**) Modeling of time-course changes of SgrS, *ptsG* mRNA, and SgrS-*ptsG* complexes. Average copy numbers per cell are plotted as a function of time. Rate constants and weighted R^2 for modeling are reported in tables S4 and S5. (**B**) Extraction of K_D for SgrS-mRNA complex formation. The ratio of mRNA in complex with SgrS to free mRNA is plotted against average SgrS copy number and the slope of the linear fitting reports $1/K_D$. Error bars in (A) and (B) report standard errors from 200 to 600 cells from two independent measurements.

Overall, our results indicate that the formation of sRNA-mRNA complexes is reversible and highly dynamic in the cell, providing additional layers for regulating individual targets. Our kinetic model highlights the importance of target search kinetics on regulation prioritization. This super-resolution imaging and analysis platform provides a conceptual framework that can be generalized to other sRNA systems and potentially to other target search processes.

REFERENCES AND NOTES

1. A. M. Gurtan, P. A. Sharp, *J. Mol. Biol.* **425**, 3582–3600 (2013).
2. S. Geisler, J. Coller, *Nat. Rev. Mol. Cell Biol.* **14**, 699–712 (2013).
3. G. Storz, J. Vogel, K. M. Wassarman, *Mol. Cell* **43**, 880–891 (2011).
4. B. Wiedenheft, S. H. Sternberg, J. A. Doudna, *Nature* **482**, 331–338 (2012).
5. A. Malkova, G. Ira, *Curr. Opin. Genet. Dev.* **23**, 271–279 (2013).
6. J. Elf, G. W. Li, X. S. Xie, *Science* **316**, 1191–1194 (2007).
7. M. Bobrovskyy, C. K. Vanderpool, *Annu. Rev. Genet.* **47**, 209–232 (2013).
8. A. Raj, P. van den Bogaard, S. A. Rifkin, A. van Oudenaarden, S. Tyagi, *Nat. Methods* **5**, 877–879 (2008).
9. B. Huang, S. A. Jones, B. Brandenburg, X. Zhuang, *Nat. Methods* **5**, 1047–1052 (2008).
10. C. K. Vanderpool, S. Gottesman, *Mol. Microbiol.* **54**, 1076–1089 (2004).
11. K. Kimata, Y. Tanaka, T. Inada, H. Aiba, *EMBO J.* **20**, 3587–3595 (2001).
12. Materials and methods are available as supplementary materials on *Science* Online.
13. H. Kawamoto, Y. Koide, T. Morita, H. Aiba, *Mol. Microbiol.* **61**, 1013–1022 (2006).
14. C. S. Wadler, C. K. Vanderpool, *Nucleic Acids Res.* **37**, 5477–5485 (2009).
15. M. Ester, H. Kriegel, J. Sander, X. Xu, in *Proceedings of the Second International Conference on Knowledge Discovery and Data Mining*, Portland, Oregon (Association for the Advancement of Artificial Intelligence, Palo Alto, CA, 1996), pp. 226–231.
16. M. Daszykowski, B. Walczak, D. L. Massart, *Chemom. Intell. Lab. Syst.* **56**, 83–92 (2001).
17. T. Morita, H. Kawamoto, T. Mizota, T. Inada, H. Aiba, *Mol. Microbiol.* **54**, 1063–1075 (2004).
18. T. Morita, K. Maki, H. Aiba, *Genes Dev.* **19**, 2176–2186 (2005).
19. E. Lubeck, L. Cai, *Nat. Methods* **9**, 743–748 (2012).
20. J. Vogel, B. F. Luisi, *Nat. Rev. Microbiol.* **9**, 578–589 (2011).
21. V. Arluison *et al.*, *Nucleic Acids Res.* **35**, 999–1006 (2007).
22. W. Hwang, V. Arluison, S. Hohng, *Nucleic Acids Res.* **39**, 5131–5139 (2011).
23. T. J. Soper, S. A. Woodson, *RNA* **14**, 1907–1917 (2008).
24. A. Fender, J. Elf, K. Hampel, B. Zimmermann, E. G. Wagner, *Genes Dev.* **24**, 2621–2626 (2010).
25. R. Hussein, H. N. Lim, *Proc. Natl. Acad. Sci. U.S.A.* **108**, 1110–1115 (2011).
26. E. Levine, Z. Zhang, T. Kuhlman, T. Hwa, *PLOS Biol.* **5**, e229 (2007).
27. D. Jost, A. Nowojewski, E. Levine, *Biophys. J.* **104**, 1773–1782 (2013).
28. J. B. Rice, C. K. Vanderpool, *Nucleic Acids Res.* **39**, 3806–3819 (2011).
29. Y. Sun, C. K. Vanderpool, *J. Bacteriol.* **195**, 4804–4815 (2013).

ACKNOWLEDGMENTS

We thank L. A. Sepulveda, L. H. So, M. Bates, X. Zhuang, Y. Liu, J. E. Stone, K. Schulten, H. Aiba, Z. Luthey-Schulten, T. E. Kuhlman, Y. Wang, and T. Lu for discussion, reagents, and software (*12*). This work was supported by grants from the National Science Foundation (PHY 082265 and PHY 1147498), the National Institutes of Health (GM 112659, GM065367, GM082837, and GM092830), the Welch Foundation (Q-1759), and the Jane Coffin Childs Memorial Fund for Medical Research.

SUPPLEMENTARY MATERIALS

www.sciencemag.org/content/347/6228/1371/suppl/DC1
Materials and Methods
Supplementary Text
Figs. S1 to S18
Tables S1 to S5
Movies S1 to S3
References (*30–54*)

16 July 2014; accepted 16 January 2015
10.1126/science.1258849

STEM CELL AGING

A mitochondrial UPR-mediated metabolic checkpoint regulates hematopoietic stem cell aging

Mary Mohrin,[1]* Jiyung Shin,[1]* Yufei Liu,[2]* Katharine Brown,[1]* Hanzhi Luo,[1] Yannan Xi,[1] Cole M. Haynes,[3,4] Danica Chen[1]†

Deterioration of adult stem cells accounts for much of aging-associated compromised tissue maintenance. How stem cells maintain metabolic homeostasis remains elusive. Here, we identified a regulatory branch of the mitochondrial unfolded protein response (UPR^{mt}), which is mediated by the interplay of SIRT7 and NRF1 and is coupled to cellular energy metabolism and proliferation. SIRT7 inactivation caused reduced quiescence, increased mitochondrial protein folding stress (PFS^{mt}), and compromised regenerative capacity of hematopoietic stem cells (HSCs). SIRT7 expression was reduced in aged HSCs, and SIRT7 up-regulation improved the regenerative capacity of aged HSCs. These findings define the deregulation of a UPR^{mt}-mediated metabolic checkpoint as a reversible contributing factor for HSC aging.

Aging is characterized by physiological decline and increased susceptibility to pathologies and mortality. The rate of aging is controlled by evolutionarily conserved genetic pathways (*1*, *2*). The general cause of aging is the chronic accumulation of cellular damage (*2*, *3*). This conceptual framework raises fundamental questions about aging. What are the origins of aging-causing damage? What is the cell or tissue specificity for sensing or responding to such damage? Are the effects of cellular damage on physiological aging reversible?

Adult stem cells mostly reside in a metabolically inactive quiescent state to preserve their integrity but convert to a metabolically active proliferative state to replenish the tissue (*4*–*6*). The signals that trigger stem cells to exit the cell cycle and enter quiescence, and the signal transduction leading to the transition, remain elusive.

SIRT7 is a histone deacetylase that is recruited to its target promoters by interactions with transcription factors for transcriptional repression (*7*). We took a proteomic approach to identify SIRT7-interacting transcription factors. We transfected human embryonic kidney–293T (HEK-293T) cells with Flag-tagged SIRT7, affinity-purified the Flag-tagged SIRT7 interactome, and identified SIRT7-interacting proteins by mass spectrometry. Among the potential SIRT7-interacting proteins was nuclear respiratory factor 1 (NRF1), a master regulator of mitochondria (*8*). Transfected Flag-SIRT7 and endogenous SIRT7 interacted with NRF1 in HEK-293T cells (Fig. 1, A and B).

SIRT7 bound the proximal promoters of mitochondrial ribosomal proteins (mRPs) and mitochondrial translation factors (mTFs) but not other NRF1 targets (Fig. 1C and fig. S1A) (*7*). NRF1 bound the same regions as SIRT7 at the proximal promoters of mRPs and mTFs but not RPS20 (Fig. 1D and fig. S1B), where SIRT7 binding is mediated through Myc (*9*). SIRT7 binding sites were found adjacent to NRF1 consensus binding motifs at the promoters of mRPs and mTFs (fig. S1C). NRF1 knockdown (KD) using small interfering RNA (siRNA) reduced SIRT7 occupancy at the promoters of mRPs and mTFs but not RPS20 (Fig. 1C and fig. S2). SIRT7 KD using short hairpin RNAs led to increased expression of mRPs and mTFs, which was abrogated by NRF1 siRNA (Fig. 2, A and B, and fig. S3). Thus, NRF1 targets SIRT7 specifically to the promoters of mRPs and mTFs for transcriptional repression.

Transcriptional repression of mitochondrial and cytosolic (*7*, *9*) translation machinery by SIRT7 suggests that SIRT7 might suppress mitochondrial activity and proliferation. SIRT7 KD cells had increased mitochondrial mass, citrate synthase activity, adenosine triphosphate levels, respiration, and proliferation, whereas cells overexpressing wild type (WT) but not a catalytically inactive SIRT7 mutant (H187Y) showed reduced mitochondrial mass, respiration, and proliferation (Fig. 2, C to E, and fig. S4, A to G) (*10*, *11*). NRF1 siRNA abrogated the increased mitochondrial activity and proliferation of SIRT7 KD cells (fig. S4, H to J). Thus, SIRT7 represses NRF1 activity to suppress mitochondrial activity and proliferation.

Sirtuins are increasingly recognized as stress resistance genes (*12*–*14*). Nutrient deprivation induced SIRT7 expression (fig. S5A). Upon nutrient deprivation stress, cells reduce mitochondrial activity, growth, and proliferation to prevent cell death (*15*, *16*). When cultured in nutrient-deprived medium, cells overexpressing SIRT7 showed increased survival, whereas SIRT7 KD cells showed reduced survival, which was improved by NRF1 siRNA (fig. S5). Thus, SIRT7 suppresses NRF1 activity to promote nutritional stress resistance.

Perturbation of mitochondrial proteostasis, a form of mitochondrial stress, activates the mitochondrial unfolded protein response (UPR^{mt}), a retrograde signaling pathway leading to transcriptional up-regulation of mitochondrial chaperones and stress relief (*17*, *18*). Mitochondrial dysfunction results in attenuated translation, which helps restore mitochondrial homeostasis (*19*). SIRT7-mediated transcriptional repression of the translation machinery suggests that SIRT7 may alleviate mitochondrial protein folding stress (PFS^{mt}). PFS^{mt} induced SIRT7 expression (Fig. 2F). Induction of PFS^{mt} by overexpression of an aggregation-prone mutant mitochondrial protein, ornithine transcarbamylase (ΔOTC), results in UPR^{mt} activation and efficient clearance of misfolded ΔOTC (*18*). In SIRT7 KD cells, misfolded ΔOTC accumulated to a higher level (Fig. 2G). SIRT7 KD cells displayed increased apoptosis upon PFS^{mt} (Fig. 2H) but are not prone to general apoptosis (*9*). Thus, SIRT7 alleviates PFS^{mt} and promotes PFS^{mt} resistance. Consistently, mitochondrial dysfunction is manifested in the metabolic tissues of SIRT7-deficient mice (*20*).

PFS^{mt} induced the expression of canonical UPR^{mt} genes in SIRT7-deficient cells (fig. S6, A and B), indicating that induction of SIRT7 and canonical UPR^{mt} genes is in separate branches of the UPR^{mt}. Untreated SIRT7 KD cells displayed increased expression of canonical UPR^{mt} genes (fig. S6, A and B), but SIRT7 did not bind to their promoters (fig. S1A) (*7*), suggesting that SIRT7 deficiency results in constitutive PFS^{mt} and compensatory induction of canonical UPR^{mt} genes. NRF1 siRNA abrogated increased PFS^{mt}, but not endoplasmic reticulum stress, in SIRT7 KD cells

---

[1] Program in Metabolic Biology, Nutritional Sciences and Toxicology, University of California, Berkeley, CA 94720, USA. [2] Department of Molecular and Cell Biology, University of California, Berkeley, CA 94720, USA. [3] Cell Biology Program, Memorial Sloan Kettering Cancer Center, New York, NY 10065, USA. [4] Biochemistry, Cell and Molecular Biology Allied Program, Weill Cornell Medical College, 1300 York Avenue, New York, NY, USA.
*These authors contributed equally to this work. †**Corresponding author. E-mail: danicac@berkeley.edu**